



1
2
3
4
5
6
7
8
9
10
11
12
13
14
15
16
17
18
19
20
21
22
23
24

Forecasting and Identifying the Meteorological and Hydrological Conditions Favoring the Occurrence of Severe Hazes in Beijing and Shanghai using Deep Learning

Chien Wang

Laboratoire d'Aerologie, CNRS and University Paul Sabatier
14 Avenue Edouard Belin, 31400 Toulouse, France

Correspondence to: Chien Wang (chien.wang@aero.obs-mip.fr)



25 **Abstract.** Severe haze or low visibility event caused by abundant atmospheric aerosols has
26 become a serious environmental issue in many countries. A framework based on deep
27 convolutional neural networks has been developed to forecast the occurrence of such events in
28 two Asian megacities: Beijing and Shanghai. Trained using time sequential regional maps of
29 meteorological and hydrological variables alongside surface visibility data over the past 41
30 years, the machine has achieved a good overall accuracy in associating the haze events with
31 favorite meteorological and hydrological conditions. Furthermore, an unsupervised cluster
32 analysis using features with a greatly reduced dimensionality produced by the trained machine
33 has, arguably for the first time, successfully categorized typical regional meteorological-
34 hydrological regimes alongside local quantities associated with haze and non-haze events in the
35 two targeted cities, providing substantial insights to advance our understandings of this
36 environmental extreme.

37 1 Introduction

38 Frequent low visibility or haze event caused by elevated abundance of atmospheric aerosols
39 due to fossil fuel and biomass burning has become a serious environmental issue in many Asian
40 countries in recent decades, interrupting economic and societal activities and causing human
41 health issues (*e.g.*, Chan and Yao, 2008; Silva *et al.*, 2013; Lee *et al.*, 2017). For example, rapid
42 economic development and urbanization in China have caused various pollution-related health
43 issues particularly in populated metropolitans such as Beijing-Tianjin region and Yangtze river
44 delta centered in Shanghai (*e.g.*, Liu *et al.*, 2017). In Singapore, the total economic cost of severe
45 haze events in 2015 is estimated to be \$510 million (0.17% of GDP), or \$643.5 million based on
46 a wiling-to-pay analysis (Lin *et al.*, 2016). To ultimately prevent this detrimental environmental
47 extreme from happening requires rigid emission control measures in place through significant
48 changes in energy consumption as well as land and plantation management. Before all these
49 measures could finally take place, it would be more practical to develop skills to accurately
50 predict its occurrence hence to allow mitigation measures to be implemented ahead of time.

51 Severe haze events arise from the solar radiation extinction by aerosols in the atmosphere,
52 this mechanism can be enhanced with the increase of relative humidity that enlarges the size of
53 particles (*e.g.*, Kiehl and Briegleb 1993). Aerosols also need favorite atmospheric transport and
54 mixing conditions to reach places away from their immediate source locations, while their
55 lifetime in the atmosphere can be significantly reduced by rainfall removal. In addition, soil
56 moisture is also a key to dust emissions. Therefore, meteorological and hydrological conditions
57 are critical to the occurrence of haze events besides particulate emissions. To forecast the
58 occurrence of such events using existing atmospheric numerical models developed based on fluid
59 dynamics and explicit or parameterized representations of physical and chemical processes, the
60 actual task is to accurately predict the concentration of aerosols at a given geographic location
61 and a given time in order to correctly derive surface visibility (*e.g.*, Lee *et al.* 2017 & 2018).
62 However, the propagation of numerical or parameterization errors through the model integration
63 could easily drift the model away from the original track, not mentioning that lack of real-time
64 emission data alone would simply handicap such an attempt. Therefore, a more fundamental
65 issue in practice is whether these models could reproduce the *a posteriori* distribution of the
66 possible outcomes of the targeted low-probability extreme events. Ultimately, lack of knowledge
67 about the extreme event would, in turn, hinder the effort to improve the forecasting skills.



68 Differing from the deterministic models, an alternative statistical prediction approach could
69 be adopted should the predictors of a targeted event could be identified and a statistical
70 correlation between them could be established with confidence. However, this is a rather difficult
71 task for the traditional approaches because it requires an analysis dealing with a very large
72 quantity of high-dimensional data in order to establish a likely multi-variate and nonlinear
73 correlation of generalization. Nevertheless, such attempts can obviously benefit now from the
74 fast-growing machine learning (ML) and deep learning (DL) algorithm development (*e.g.*,
75 LeCun *et al.*, 2015). In addition, technological advancement and continuous investment from
76 governments and other sectors across the world have led to a rapid increase of quantity alongside
77 substantially improved quality of meteorological, oceanic, hydrological, land, and atmospheric
78 composition data. These data might still not be sufficient for evaluating and improving certain
79 detailed aspects of the deterministic forecasting models. However, rich information contained in
80 these data about favorite environmental conditions for the occurrence of extreme events such as
81 hazes could already have a great value for developing alternative forecasting skills.

82 Many Earth science applications dealing with meteorological or hydrological data need a
83 trained machine to not only forecast values but also recognize patterns or images. However, this
84 can easily lead to a curse of dimensionality of many traditional ML algorithms. Fortunately, deep
85 learning that directly links large quantity of raw data with targeted outcomes through deep
86 convolutional neural networks or CNNs (Goodfellow *et al.*, 2016) offers a clear advantage in
87 sufficiently training deep networks suitable for solving highly nonlinear issues. In doing so, DL
88 can also eliminate the possible mistakes in data derivation or selection introduced by subjective
89 human opinion regarding a poorly understood phenomenon. Recently, DL algorithms have been
90 explored in various applications in atmospheric, climate, and environmental sciences, ranging
91 from recognizing specific weather patterns (*e.g.*, Liu *et al.*, 2016; Kurth *et al.*, 2018; Lagerquist
92 *et al.*, 2019; Chattopadhyay *et al.*, 2020), weather forecasting including hailstorm detection (*e.g.*,
93 Grover *et al.*, 2015; Shi *et al.*, 2015; Gagne *et al.*, 2019), to deriving model parameterizations
94 (*e.g.*, Jiang *et al.*, 2018), and beyond.

95 When weather patterns associated with targeted outcome are known or irrelevant to the task,
96 the forecasting can be normally proceeded to recognize a given pattern by using pattern-to-
97 pattern correlation from sequential training data with spatial-information-preserving full CNNs
98 such as U-net (Ronneberger *et al.*, 2015; Weyn *et al.*, 2020). However, this is certainly not the
99 case for the applications where the environmental conditions associated with targeted outcome
100 are yet known. For such applications, a possible solution is to utilize a large quantity of raw data
101 with minimized human intervention in data selection to train a deep CNN in order to associate
102 targeted outcomes with favorite environmental conditions. This study represents such an attempt,
103 where a DL forecast framework is trained to identify the meteorological and hydrological
104 conditions associated with the occurrences of severe hazes. The DL framework has been
105 developed initially with the severe hazes in Singapore (Wang, 2020), and now hazes in two
106 megacities of China, Beijing and Shanghai. In terms of particulate pollutant emissions, all these
107 cities share certain sources including fossil fuel combustions from transportation, domestic, and
108 industries. On the other hand, each city also has its own unique sources, for instance, desert and
109 perhaps anthropogenic dust for Beijing, and massive biomass burning in Singapore (Chen *et al.*,
110 2013; Liu *et al.*, 2017; Lee *et al.*, 2017, 2018, & 2019). It is obvious that besides meteorological
111 and hydrological conditions, dynamical patterns of anthropogenic activities leading to the
112 emissions of particulate matters are also important factors behind the occurrence of severe hazes.
113 Nevertheless, the major purpose of this study is to advance our fundamental knowledge about the

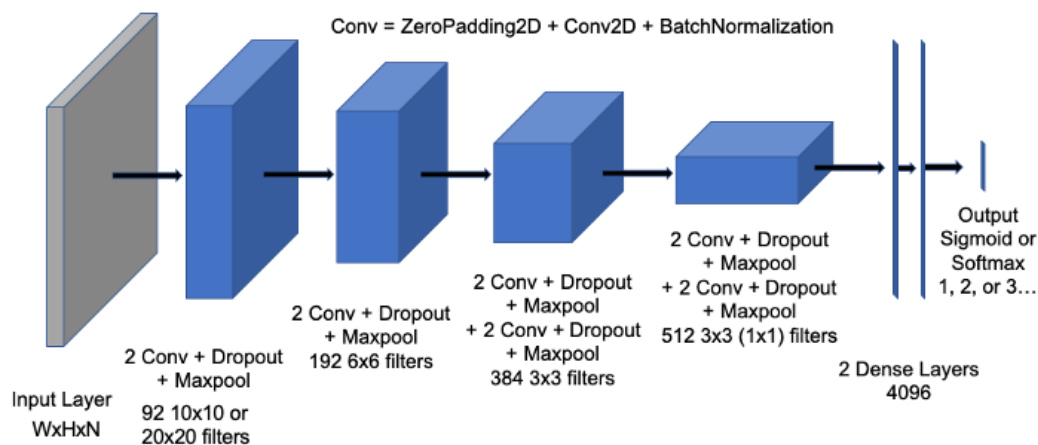


114 weather conditions favoring the occurrence of hazes and, through an in-depth analysis on the
115 forecasting results to identify the limit of such a machine and thus to provide useful information
116 for establishing a more complete forecasting platform for the task.

117 In the paper, the architecture alongside method and data for training are firstly described after
118 this Introduction, followed by a discussion of training and validation results. Then, an
119 unsupervised cluster analysis benefited from the trained machine is introduced along with the
120 results that furthers the understanding of the CNN's performance and summarizes, for the first
121 time, the various typical meteorological and hydrological regimes associated with haze versus
122 non-haze situations in the two cities. The last section concludes the major efforts and findings.

123 2 Network Architecture, Training Methodology and Data

124 The convolutional neural network used in this study, the HazeNet (Wang 2020), has been
125 developed by adopting the general architecture of the CNN developed by the Oxford
126 University's Visual Geometry Group or VGG-Net (Simonyan and Zisserman, 2015). The actual
127 structure alongside hyper-parameters of HazeNet have been adjusted and fine-tuned based on
128 numerous test trainings. In addition, certain techniques that were not available when the original
129 VGG net was developed, *e.g.*, batch normalization (Ioffe and Szegedy, 2015), have been
130 included as well. The current version for haze applications of Beijing and Shanghai contains
131 20,507,161 parameters (11,376 non-trainable). Figure 1 shows the general architecture of a
132 HazeNet version with 12 convolutional and 4 dense layers (in total 57 layers).



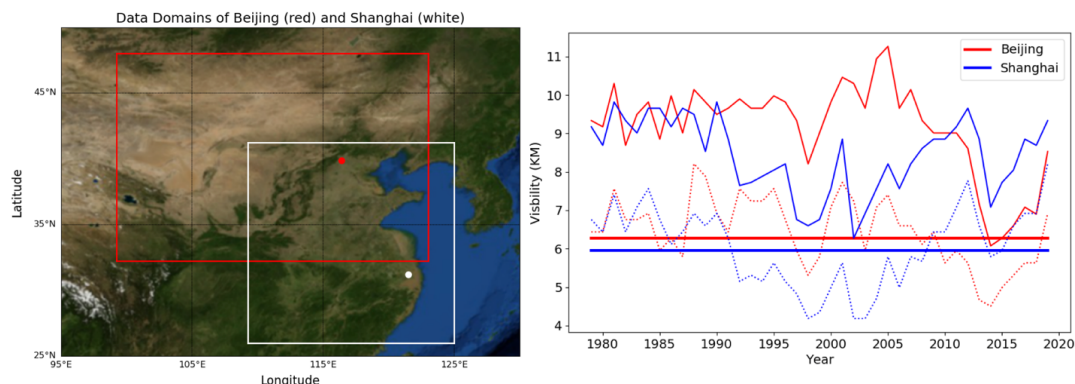
133 **Figure 1.** Architecture of the 12 convolutional plus 4 dense layer HazeNet. Here “Conv” represents a unit
134 containing a zero-padding then a 2D convolutional layer, followed by a batch normalization layer. There
135 is a flatten layer before the 2 dense layers. W = width, H = height, and N = number of features of the
136 input fields, they are 64, 96, and 16 for Beijing, and 64, 64, and 16 for Shanghai case, respectively.
137

138 The network has been trained in a standard supervised learning procedure for classification.
139 In this procedure, the network takes input features to produce classification output that are then
140 compared with known results or labels based on observations. The coefficients of the network
141 are thereafter optimized in order to minimize the error between the prediction and the



142 observation or label. The loss function used in optimization is cross-entropy (*e.g.*, Goodfellow *et*
143 *al.*, 2017). Such a procedure is repeated until the performance of the network can no longer be
144 improved. In practice, the trainings usually last about 2000 epochs (each epoch is a training cycle
145 that uses up the entire training dataset). This procedure in nature is to train a deep CNN to
146 recognize then associate input features (bundled meteorological and hydrological conditions in
147 this case) with corresponding class, *i.e.*, severe haze events or non-haze events. As a result, the
148 knowledge specifically about the favorite meteorological and hydrological conditions of severe
149 hazes could be advanced.

150 The labels for the training are derived using the observed daily surface visibility (*vis.*
151 thereafter), obtained from the Global Surface Summary Of the Day or GSOD dataset consisting
152 of daily observations of meteorological conditions from tens of thousands of airports around the
153 globe (Smith *et al.*, 2011). In the cases of Beijing and Shanghai, data are from the time period
154 from 1979 to 2019, containing 14975 samples. For simplicity, the discussions will be mainly on
155 the 2-class training, where events with $vis. \leq$ the long-term mean value of the 25th percentile or
156 p25 of *vis.* (6.27 km in Beijing, 5.95 km in Shanghai; Fig. 2, right panel; also Fig. S1 in
157 Supplementary) are defined as class 1 or severe hazes, otherwise the class 0 or non-haze cases.
158 The p25 values actually represent a substantial reduction of *vis.* due to high particulate pollution
159 (*e.g.*, Lee *et al.*, 2017). Note that unlike in the case of Singapore (Wang 2020), fog and mist are
160 more common low visibility events in Beijing and Shanghai and thus have been excluded from
161 the labels of severe hazes by following GSOD fog marks. The number of severe haze events
162 occurred during 1979-2019 defined in the above procedure is 2999 and 3099 for Beijing and
163 Shanghai, or in a frequency of 20.0% and 20.7%, respectively.



164
165 **Figure 2.** (Left) The input-feature defining domains for Beijing (red box and dot, 99.25 - 123E, 32.25-
166 48N; 96x64 grids with ERA5 data) and Shanghai (white box and dot, 109.25-125E, 26-41.25N; 64x64
167 grids), made using Basemap library, a matplotlib extension. (Right) Annual means (solid curves), 25th
168 percentiles (dash curves), and 25th percentile means (solid straight lines) of surface visibility in Beijing
169 (red) and Shanghai (blue) between 1979 and 2019.

170 The training and validation of HazeNet also need the input features with the same sample
171 dimension of the labels. These input data are derived from hourly longitude-latitude maps of
172 meteorological and hydrological variables covering the data collection domain (Fig. 2, Left),
173 obtained from ERA5 reanalysis data produced by the European Centre for Medium-range
174 Weather Forecasts or ECMWF (Hersbach *et al.*, 2020). These data are distributed in a grid
175 system with a horizontal spatial interval of 0.25 degree. Up to 16 features are derived from the
176 original hourly data fields covering the analysis domain respectively for Beijing (64x96 grids)



177 and Shanghai (64x64 grids), including: daily mean of surface relative humidity (REL thereafter);
178 diurnal change as well as daily standard deviation of 2-meter temperature or DT2M and T2MS,
179 respectively; daily mean of 10-meter zonal and meridional wind speed or U10 and V10,
180 respectively; daily mean of total column water (TCW); daily mean (TCV) and diurnal change
181 (DTCV) of total column water vapor; daily mean of planetary boundary layer height (BLH);
182 daily mean soil water volume in soil layer 1 and 2 or SW1 and SW2, respectively; daily mean of
183 total cloud cover (TCC); daily mean geopotential heights at 500 (Z500) and 850 (Z850) hPa
184 pressure levels along with their diurnal changes D500 and D850, respectively. All input features
185 have been normalized into a range of [-1, +1] (Fig. S2 in Supplementary).

186 Before the training, the entire samples of labels alongside corresponding input features were
187 randomly shuffled first then split as: 2/3 of the samples went to training set and 1/3 to validation
188 set, each is used duly for its designated purpose throughout the entire training process without
189 switch. The above procedure treats each of the events as an independent one. For the
190 convenience in comparing performance or restarting training based on a saved machine, a pair of
191 saved training and validation datasets produced following the above procedure was used.

192 The number of samples used in training HazeNet is rather limited in deep learning standard.
193 However, to associate 16 joint two-dimensional maps with targeted labels even with the current
194 number of samples is still a demanding task, requiring a deep CCN to accomplish. Furthermore,
195 targeted severe hazes are a low probability event. Its frequency of appearance is about 20.0% in
196 Beijing and Shanghai cases. Therefore, trained machine would easily bias toward the
197 overwhelming non-haze events. To resolve these issues, a combination of class-weight and batch
198 normalization has been implemented in HazeNet. This approach has effectively reduced the
199 overfitting while overcome the data imbalance issue, making the long training of a deep CNN
200 become possible (Wang, 2020).

201 3 Training and Validation Results of Haze Forecasting

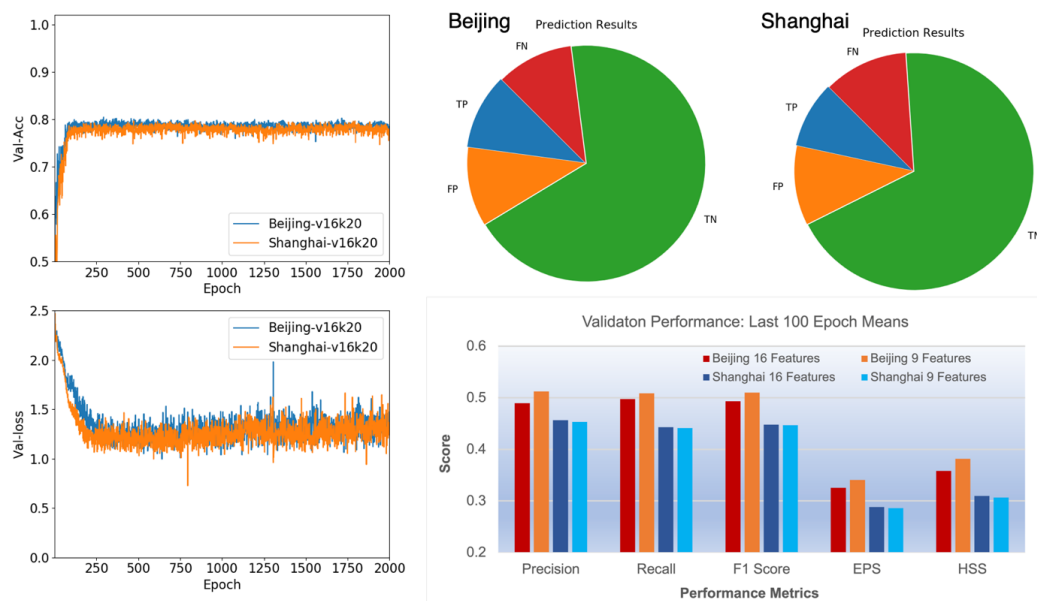
202 Currently, it is still difficult to find any practical score in forecasting the occurrence of severe
203 hazes for comparison. Therefore, the performance of HazeNet has been mainly measured by
204 using certain commonly adopted metrics for classification largely derived from the concept of
205 the so-called confusion matrix (e.g., Swets, 1988; Table A), including *accuracy*, *precision*,
206 *recall*, *F1 score*, *equitable threat score* or *ETS*, and *Heidke skill score* or *HSS* (Appendix A).
207 Unless otherwise indicated, the discussions on the performance scores are hereafter referring to
208 the severe haze class, or class 1, and obtained from validation rather than training. In all the
209 cases, the performance metrics referring to non-haze or class 0 has much better scores.

210 In order to train a stable machine, trainings with 2000 epochs or longer have been conducted
211 instead of using certain commonly used skills such as early stop. As a result, the validation
212 performance metrics of the trained machines all appeared to be stabilized by approaching the end
213 of training (Fig. 3). These scores were consistent with the results of ensemble training with the
214 same configuration but different randomly selected training and validation datasets, and also
215 comparable among trainings with different configurations. Overfitting has been clearly overcome
216 due to such a long training procedure alongside the adoption of class0weight and batch
217 normalization. In a 2-class classification (haze vs. non-haze), trained deep HazeNet can always
218 reach an almost perfect training accuracy (e.g., 0.9956 for Beijing cases) and a validation
219 accuracy of 80% in both Beijing and Shanghai cases, or the no-skill forecast accuracy for no-
220 haze (Fig. 3, left). At the same time, the performance scores in predicting specifically severe



221 hazes are also very reasonable, *e.g.*, for Beijing cases either precision or recall exceeds 0.5 (they
222 normally evolve in opposite direction), leading to a nearly 0.5 *F1 Score* (Fig.3, right). The
223 corresponding scores in training are obviously much higher, *e.g.*, with precision, recall, and F1 as
224 0.9804, 0.9980, and 0.9880, respectively for Beijing cases, owing to the deep and thus powerful
225 CNNs. HazeNet performed slightly better than several known deep CNNs such as Inception Net
226 V3 (Szegedy *et al.*, 2015), ResNet50 (He *et al.*, 2015), and VGG-19 (Simonyan and Zisserman,
227 2015) in the same haze forecasting task (Wang, 2020). Nevertheless, as indicated previously that
228 a nearly perfect validation performance is not realistic since meteorological and hydrological
229 conditions are not the only factors behind the occurrence of haze events.

230



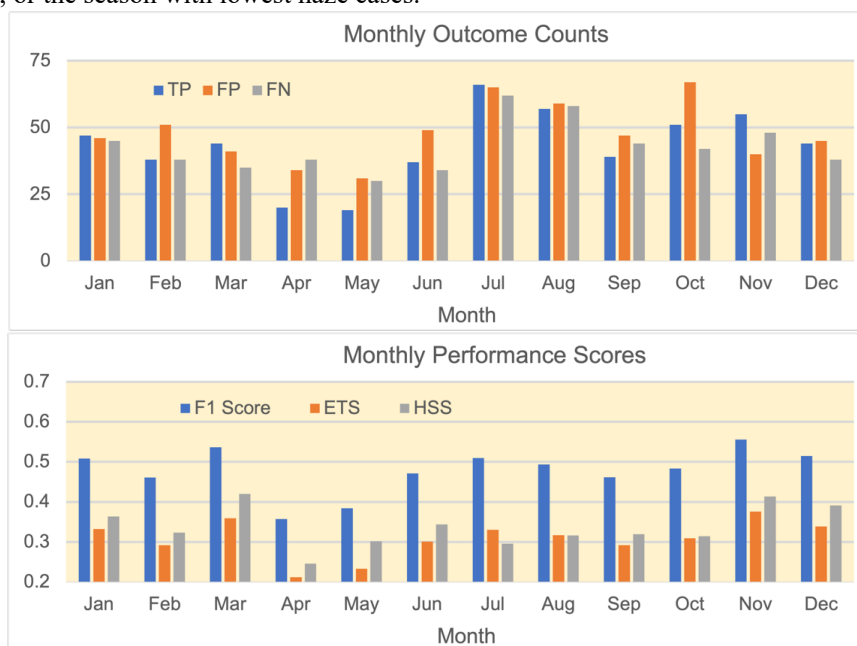
231
232 **Figure 3.** (Left) Validation accuracy (top panel) and loss (lower panel) of HazeNet with 16 features for
233 Beijing and Shanghai cases, kernel size for the first filter is 20x20. (Right Top) Prediction outcomes in
234 reference to haze events or class-1 of Beijing and Shanghai. Here TP = true positive, TN = true negative,
235 FP = false positive, and FN = false negative prediction outcomes. (Right Bottom) Scores of performance
236 metrics as last 100 epoch means for Beijing and Shanghai with 16 and 9 features, respectively.

237 Looking into the specific prediction outcomes in referring to severe haze, the trained machine
238 has produced considerably higher ratio of true positive or TP outcomes than in the Southeast
239 Asia cases (Wang, 2020) despite a number of outcomes of false positive or FP (*i.e.*, false alarm)
240 and false negative or FN (*i.e.*, missing forecast). In forecasting the severe hazes in Beijing, the
241 trained machine performs reasonably well throughout all months except for April and May or the
242 major dusty season there, producing F1 score, ETS, and HSS all exceed or near 0.5 as well as the
243 number of TP outcomes is higher than that of FN (Fig. 4). The performance of HazeNet actually
244 improves in months with higher observed haze events. For Beijing, the lowest haze season is
245 during the dusty April and May when all the major performance metrics are lower than 0.4, and
246 the machine produces more missing forecasts than true positive outcomes. The relatively poor
247 performance in spring suggests that the weather and hydrological features associated with dust-



248 dominated haze events during this period might differ from the situations in the other seasons
249 when hazes are mainly caused by local particulate pollution. For Shanghai cases, HazeNet
250 performs better during late autumn and entire winter (from November to February) when haze
251 occurs most frequently. The worst performance comes from the monsoon season (July to
252 October), or the season with lowest haze cases.

253



254

255

256

Figure 4. (Top) Predicted TP, FP, and FN outcomes and (Bottom) performance scores for each month. All from validation of Beijing cases with 16 features.

257

258

259

260

261

262

263

264

265

266

267

268

269

270

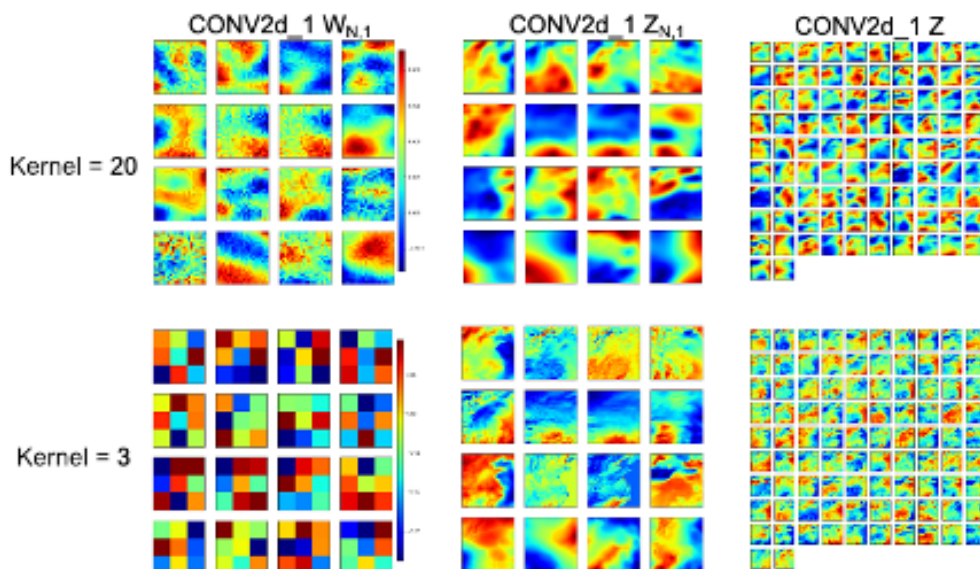
271

272

273

274

Kernel size and CNN performance. The deep architecture of HazeNet and the long training procedure have actually made the performance less sensitive to many hyperparameters of the network. One hyperparameter, however, is specifically interesting to explore for an application using large quantity of meteorological maps, that is the kernel size of the first convolutional layer, where the input data, *i.e.*, meteorological and hydrological maps are convoluted then propagated into the subsequent layers. Meteorological maps or images often contain characteristic patterns with different spatial scales. Intuitively, preserving these patterns could be important in predicting the targeted extremes. Apparently, a larger kernel size produces smoother output images from the first convolutional layer, while a smaller kernel size can preserve many spatial details of the meteorological maps as demonstrated from the layer output shown in Fig. 5. In practice, however, the patterns produced by the latter configuration might be too complicated for the networks to recognize and to perform classification, whereas patterns resulted from a relatively larger kernel size for the first convolutional layer might be more characteristic for the task. The actual result suggests that HazeNet configured with a first-layer kernel size of 20 to 26 or close to 5 – 6 degree in spatial ‘resolution’, consistently produces a better performance (about a 10% improvement in *F1 score*) than that by a smaller kernel size of 3 or 6. As a result, a kernel size of 20 has been adopted as the default configuration for the first 2 convolutional layers in this study.



275
276 **Figure 5.** (Left column) Weight coefficients of the first filter set ($W_{N,1}$), (Middle column) partial output
277 for each feature ($Z_{N,1}$), and (Right column) the output (Z) of the first convolution layer (CONV2d_1) with
278 two selected kernel sizes or ks: (upper panels) 20x20 and (lower panels) 3x3. Here W represents the filters
279 and Z the output of convolution, the subsets of Z before the feature dimension is merged can be expressed
280 as: $Z_{N,i} = W_{N,i}(ks, ks) \cdot f_N^T(ks, ks)$, with the order of input features $N = 1, \dots, 16$ and i represents the
281 convolutional layer index, *i.e.*, 1 is the first layer or CONV2d_1. For the first layer, input feature size is
282 $(h, w) = (64, 64)$, the sets of filters is 92, thus the final output Z has a dimension of $(h-ks+1, w-ks+1, 92)$.
283 Shown are results from the trainings for Shanghai haze cases.

284 **Reducing the number of input features.** One recognized advantage of deep CNN in
285 practice is its capacity to directly link the targeted outcome with a large quantity of raw data to
286 avoid human misjudgment in selecting and abstracting input features due to a lack of knowledge
287 about the application task. Nevertheless, for an application such as this one that uses a large
288 number of meteorological and hydrological variables (or channels in machine learning term),
289 reducing the number of input features with minimized influence on the performance can still
290 benefit the efforts of establishing physical or dynamical causal relations and beyond.

291 There are certain available methods to rank feature then reduce some unimportant ones.
292 These do not work straightforwardly for deep CNNs (*e.g.*, McGovern *et al.*, 2019). In the
293 previous effort, this has been done by testing the sensitivity of the full network performance in
294 real training with either a single feature or all but one features (Wang, 2020), which apparently is
295 also a demanding task. Here, another attempt has been made to use a trained then saved machine
296 to examine the sensitivity of the network to various features (Appendix B).

297 The sensitivity analyses for Beijing and Shanghai cases have obtained largely consistent
298 results, indicating that the network is more sensitive to the same 9 features than the other 7 (Fig.
299 S3). The highest-ranking features though differ, with diurnal change of column vapor (DTCV)
300 and soil water content in the second soil layer (SW2) as the most sensitive features for Beijing,
301 while relative humidity (REL) and planetary boundary layer height (BLH) for Shanghai. Most
302 importantly, trainings using only the top 9 most sensitive features have produced a performance
303 equivalent to or even better than the same training but with 16 features (Fig. 3). With reduced



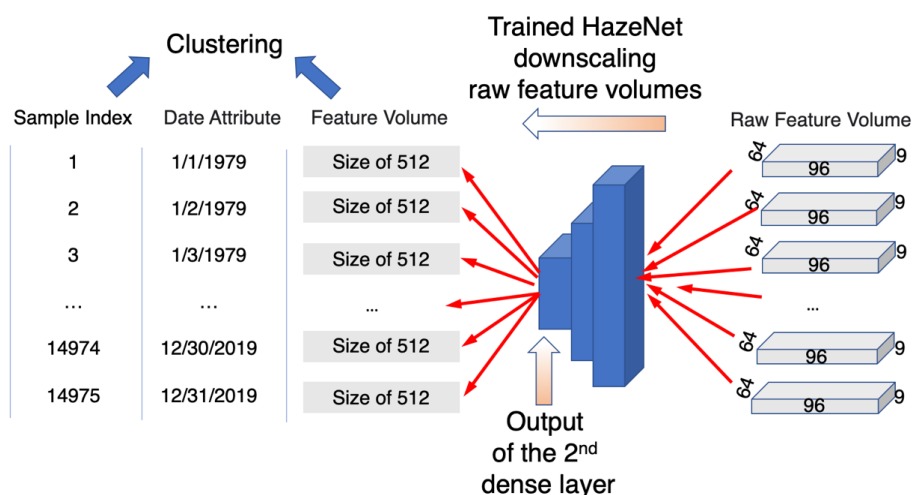
304 number of features, many further analyses can be conducted with less workload and produce
305 results that are easily understood.

306 4 Identifying and Categorizing the Typical Regional Meteorological and Hydrological 307 Regimes Associated with Haze and Non-Haze Events

308 A major purpose of this study is to identify the meteorological and hydrological conditions
309 favoring the occurrence of severe hazes in the targeted cities. When using a dataset with a large
310 number of samples, this type of analyses could be better accomplished by applying, *e.g.*, cluster
311 analysis (*e.g.*, Steinhaus, 1957), a standard unsupervised ML algorithm that groups data samples
312 into various clusters in such a way that samples in the same cluster are more similar to each other
313 than to those in other clusters. Specifically for this study, the derived clusters would likely
314 represent various regimes in terms of combined meteorological and hydrological conditions for
315 associated events. However, applying cluster analysis directly to a large number of samples, each
316 with a feature volume of ~ 50000 is an uneasy task. A dimensionality reduction is apparently
317 needed to reduce the feature volume of data.

318 In practice, a trained CNN is actually an excellent tool for this purpose. It encodes
319 (downscales) the input with large feature volume into data with a much smaller size in the so-
320 called latent space (*i.e.*, the output of the layer before the output layer) while equal predictability
321 for the targeted events. This feature has been used in developing various generative DL
322 algorithms from variational autoencoder or VAE to different generative adversarial networks or
323 GANs (*e.g.*, Forest, 2019). Therefore, the trained HazeNet for Beijing and Shanghai have been
324 used in this study to produce data with reduced size suitable for clustering (Fig. 6; see also
325 Appendix C). The new sample-feature set with a size of 14975×512 produced from this
326 procedure was then used in cluster analysis.

327



328 Figure 6. A diagram of the cluster analysis procedure. Here 96, 64, and 9 represent the number of
329 longitudinal, latitudinal grids, and number of features (variables), or the size of the input feature volume
330 of a trained HazeNet for Beijing cases, while 512 is the size of the output from the second dense layer of
331 HazeNet or the new feature volume.
332



333 In order to provide useful information for understanding the performance of the trained
334 networks, the clustering has been performed for each of the prediction outcomes rather than just
335 haze versus non-haze events (Appendix C). In this configuration, haze associated regimes are
336 represented by derived clusters of TP plus FN outcomes, while non-haze regimes by those of TN
337 plus FP. Since the clusters were actually derived using the indices of samples as the record for
338 members, the actual feature maps of the members in any cluster thus can be conveniently
339 retrieved then used to identify the representative regimes in terms of combined 9 meteorological
340 and hydrological features of various prediction outcomes or haze versus non-haze events. Here
341 the clustering results have been analyzed using the feature maps in both normalized (machine
342 native) and unnormalized (original reanalysis data) format. The characteristics of various
343 regimes can be easily identified from the former as they represent anomalies to climatological
344 means. An added benefit is to advance the understanding of the performance of the trained
345 networks. The analysis using the latter maps aims to better appreciate the conventional regional
346 and local meteorological and hydrological patterns associated with various regimes. The feature
347 maps used in both analyses have been averaged across each cluster for clarity.

348 4.1 Results based on normalized feature maps

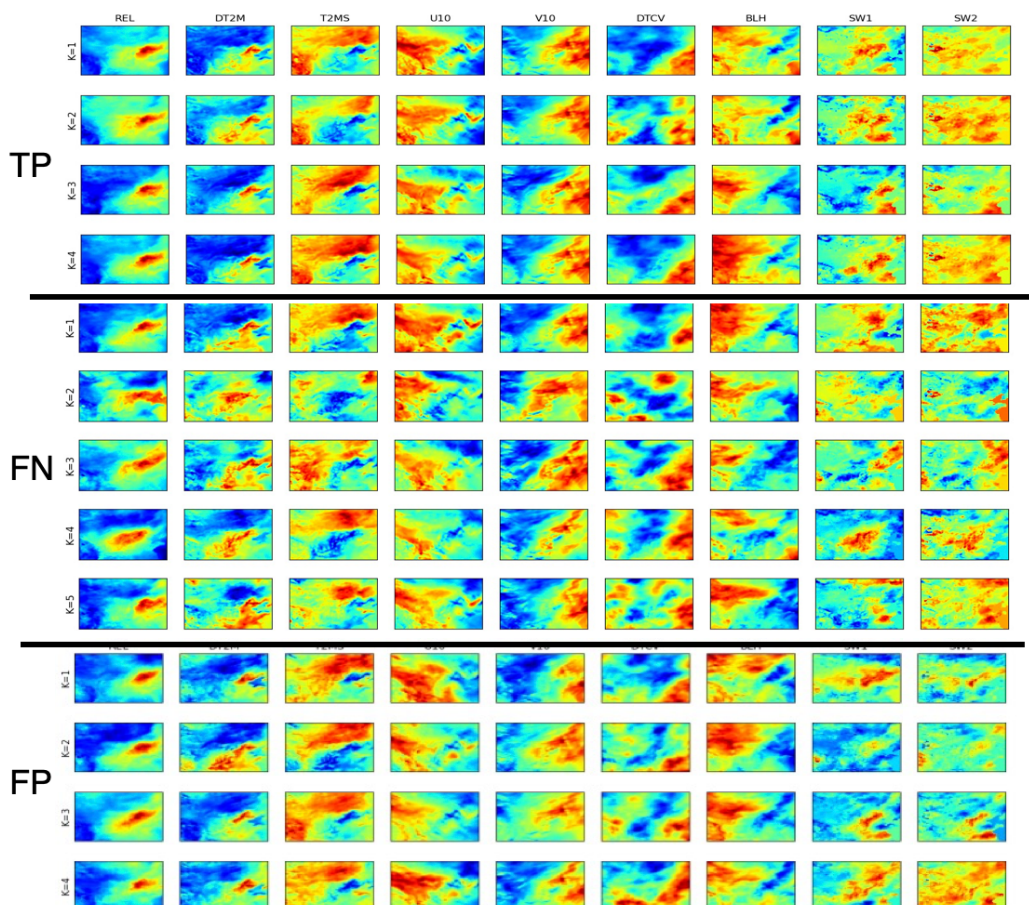
349 As shown in Figure 7, the 4 clusters of true positive or TP in Beijing cases exhibit a clear
350 similarity in general feature patterns among themselves, differing only in rather minor details.
351 The differences between clusters are more evident in the daily change of column water vapor or
352 DTCV and in two soil water contents (SW1 and SW2). On the other hand, FN clusters (also
353 associated with haze events but missed in prediction) also display a clear similarity to the
354 patterns of TP clusters across most features except DTCV, SW1, and SW2.

355 Generally speaking, the common patterns in normalized feature maps shared by most clusters
356 associated with observed haze events (*i.e.*, TP plus FN outcomes) include an isolated positive
357 relative humidity (REL) center in the southeast region covering Beijing associated with mild
358 temperature variations (DT2M and T2MS) as well as zonal wind (U10) and lower boundary
359 layer height (BLH). Note that the mild daily temperature variation alongside lower BLH
360 indicates that the haze region is not experiencing drastic weather system change such as fronts
361 and likely covered by low cloud, hence the high REL can be easily formed. All these characters
362 reflect a stable regional weather conditions over the southeastern half of the domain where
363 targeted hazes occurred. They are also in a sharp contrast to the conditions in the northwestern
364 half of the domain as well as the conditions associated with non-haze events represented by TN
365 outcomes (Fig. S4).

366 Interestingly, the 4 FP (false alarm) clusters actually display a similarity in normalized
367 feature patterns to those of TP as those of FN (Fig. 7). In addition, despite an anticipated
368 diversity in feature patterns across TN clusters (Fig. S4), four of its clusters (*i.e.*, 2, 5, 12, and 13)
369 exhibit a certain level of similarity to those of TP clusters. All these could offer an explanation
370 for the forecast errors made by the machine, *i.e.*, the machine could have simply been confused
371 by such similarities between certain FN and TN members, or between certain TP and FP
372 members. Nevertheless, these could also suggest an alternative reason behind the incorrect
373 forecasts. It is worth indicating again that meteorological or hydrological conditions are not the
374 only factors determining the occurrence of hazes. Other factors such as abnormal energy
375 consumption events or long-range transport of aerosols could all cause haze to occur even under
376 unfavorable weather and hydrological conditions. This could well be the reason for some of the
377 missing forecasts (FN outcomes) when haze occurred under unfavorable conditions, or for false



378 alarms (FP outcomes) when low aerosol events occurred even under a weather condition
379 favorable to haze. Future improvement of the skill could benefit from this knowledge.
380 The results of Shanghai are largely the same as in Beijing case (Fig S5 & S6).



381
382 **Figure 7.** Maps of 9 features in normalized format for 4 clusters of true positive or TP outcome,
383 5 clusters of false negative or FN outcome, and 4 clusters of false positive or FP outcome. Here TP plus FN = haze
384 events. Results shown are cluster averages for Beijing cases.

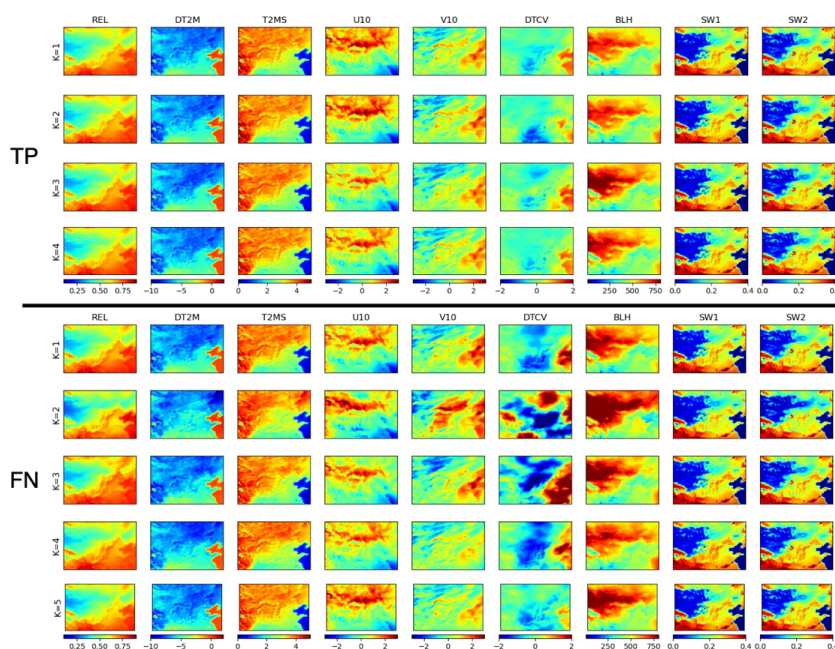
385 4.2 Results based on original unnormalized feature maps

386 Utilizing feature maps in their original unnormalized format represented by actual physical
387 quantities could provide a convenience to appreciate the conventional regional and local
388 meteorological and hydrological patterns associated with various events. Note that the visual
389 differences between unnormalized feature maps particularly in cluster-mean format might be
390 subtle for bare eyes to recognize.

391 For haze events in Beijing (*i.e.*, TP and FN outcomes; Fig. 8), the associated cluster-mean
392 regional meteorological and hydrological patterns of most features except DTCV contain two
393 regions with sharply contrasting quantities, roughly separated by a line linking the southwest and
394 northeast corner of the domain, likely due to the nature of weather system besides meridional



395 variation of general climate. Beijing (at $\sim 1/3$ domain width from the east boundary and nearly
396 the north-south center) locates in the southeastern half of the domain. In comparison, as same as
397 shown in the previous analysis using normalized feature maps, the patterns of FN clusters share
398 many common patterns with those of TP clusters. Their differences are more evident in DTCV,
399 SW1, and SW2. In addition, cluster 5 of FN shows more diverse patterns than the rest. FP
400 clusters also display a similarity to those of TP clusters (Fig. S5), whereas TN clusters show
401 more visible differences particularly in patterns of meridional wind (V10) and daily change of
402 column water vapor or DTCV (Fig. S6).



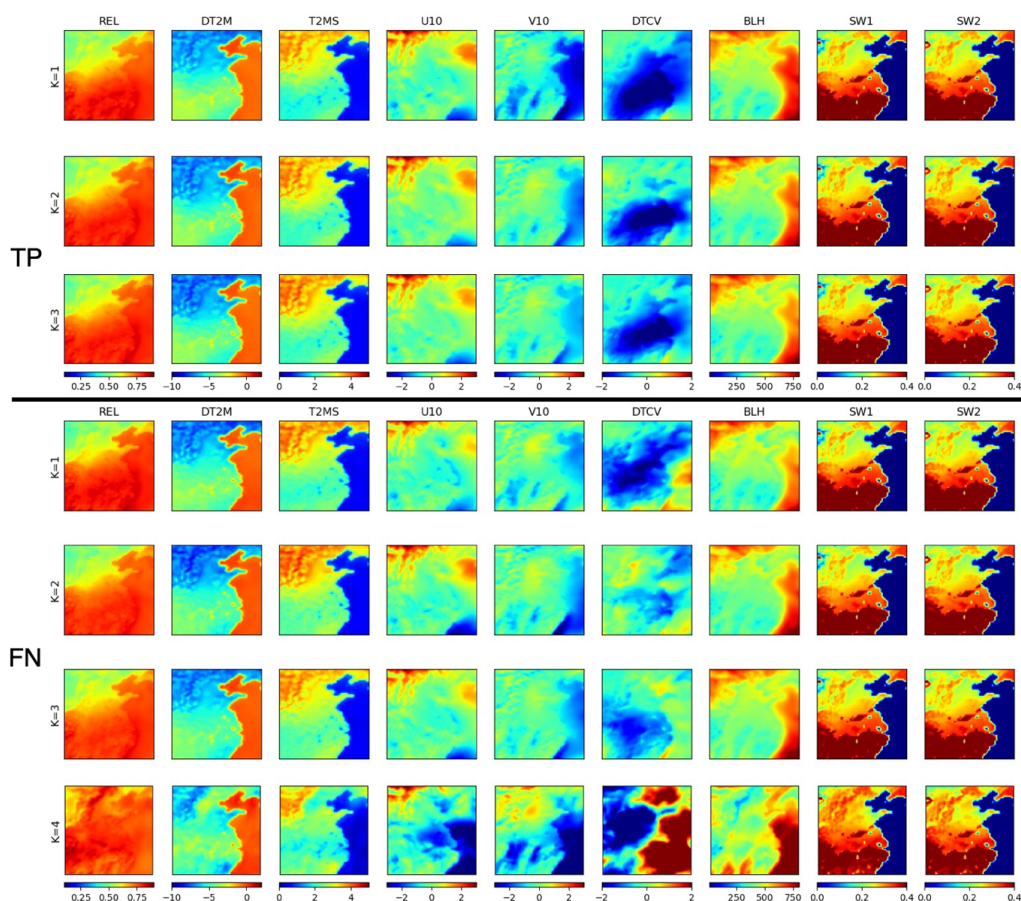
403

404 **Figure 8.** Feature maps associated with severe haze events in Beijing represented by 4 clusters of TP (4
405 top rows) and 5 clusters of FN (5 lower rows) predicted outcomes. Shown are cluster means of
406 unnormalized data of REL (ratio), DT2M and T2MS in degree, U10 and V10 in m/s, DTCV (kg/m^2),
407 BLH in meter, and SW1 and SW2 in kg/m^2 .

408 The general regional meteorological and hydrological conditions during haze events in the
409 southeastern in comparison to the northwestern portion of the domain include a higher relative
410 humidity, lower variation of surface temperature, largely northward or northwestward wind,
411 lower planetary boundary layer height, and higher soil water content, and quantity wise these are
412 all in a sharp contrast to the situations in the other half of the domain. The visually recognized
413 cross-cluster differences of haze events mainly exist in DTCV patterns, represented by a strong
414 negative center in the middle of the domain with varying extent across different clusters. To a
415 less extent, patterns of surface wind V10 and U10 also offer some different characteristics
416 among various clusters particularly of FN clusters. Consistent to the analysis result using
417 normalized feature maps, all these indicate a stable weather condition over the southeastern half
418 of the domain for haze events in Beijing. It is known that dust can cause low visibility events in
419 Beijing. During dust seasons, the condition of the northwestern half of the domain, represented
420 by a dominant eastward wind and lower soil water content likely favors dust transport from



421 desert to Beijing. However, the details would need an in-depth analysis to examine since most
422 clusters having members rather well distributed through different months.
423 The cluster-means of 9 features for haze events (TP plus FN) versus non-haze (TN plus FP)
424 at the grid point of Beijing are also derived and listed in Table 1 for reference. Specifically, the
425 common local conditions associated with hazes in Beijing in comparison to those with non-haze
426 events include a higher humidity, less drastic variations in surface temperature, a northwestward
427 rather than southeastward wind, a lower planetary boundary layer height, and higher soil water
428 contents. Again, the most recognizable cross-cluster differences appear in DTCV, followed by
429 surface wind. In most of the local features, variabilities of FN clusters tend to be larger than
430 those of TP clusters. One interesting result of the local weather conditions shown in Table 1 is
431 that the cluster means of TN are sharply different than those of TP and FN, while the cluster
432 means of FP and those of TP+FN are likely to be statistically indifferent except for DTCV,
433 providing an evidence to support the assumption that FP outcomes might simply represent the
434 non-haze events caused by reasons other than weather and hydrological conditions.
435



436
437
438

Figure 9. The same as Figure 9 except for Shanghai with 3 clusters for TP and 4 for FN outcomes.



439 For the case of Shanghai, the general weather conditions associated haze events are likely
 440 stable, with characters similar to the cases of Beijing (Fig. 9). Quantities of most feature patterns
 441 display a sharply southeast versus northwest contrast. DTCV maps display a negative center over
 442 a large area, its distribution and extent vary significantly among different clusters. The patterns
 443 of soil water content in both soil layers exhibit a sharp meridional contrast, much higher in the
 444 south part of the domain than in the north part, largely separated by the Yellow River. Local
 445 quantities of all the features associated with haze events (TP plus FN) in Shanghai display clear
 446 differences with those of non-haze prediction outcomes (TN) (Table 1). Similar to the cases of
 447 Beijing, the cluster mean of the FP outcomes is statistically indifferent to those of haze (TP and
 448 FN) than predicted non-haze (TN) events. Again, this result implies that even a weather pattern
 449 favoring haze appeared and was correctly recognized by HazeNet, due to other factors such as
 450 energy consumption variations, haze could still not to occur.

451 **Table 1.** Cluster means of features associated with haze events (TP and FN) in Beijing and Shanghai
 452 versus means of all clusters of non-haze events of TN and FP, respectively. Number of cluster members
 453 of each cluster are listed in bracket.

<i>Cluster</i>	<i>REL</i> (0-1)	<i>DT2</i> (°C)	<i>T2MS</i> (°C)	<i>U10</i> (m/s)	<i>V10</i> (m/s)	<i>DTCV</i> (kg/m ²)	<i>BLH</i> (m)	<i>SW1</i> (kg/m ²)	<i>SW2</i> (kg/m ²)
<i>Beijing</i>									
<i>TP1 (848)</i>	0.64	-5.99	3.24	-0.29	0.20	0.04	379.71	0.23	0.22
<i>TP2 (181)</i>	0.65	-5.80	3.14	-0.28	0.19	0.57	378.33	0.23	0.23
<i>TP3 (354)</i>	0.65	-5.39	2.98	-0.45	0.29	0.31	400.20	0.23	0.22
<i>TP4 (1208)</i>	0.64	-5.82	3.18	-0.34	0.28	0.27	381.28	0.23	0.22
<i>FN1 (157)</i>	0.66	-5.83	3.16	-0.43	0.34	0.15	379.91	0.23	0.21
<i>FN2 (13)</i>	0.65	-5.05	2.98	-0.52	0.48	-1.88	422.35	0.23	0.22
<i>FN3 (29)</i>	0.69	-5.90	3.05	-0.41	0.36	0.99	393.52	0.24	0.23
<i>FN4 (86)</i>	0.64	-5.64	3.02	-0.19	0.11	0.10	420.49	0.23	0.22
<i>FN5 (223)</i>	0.60	-6.56	3.45	-0.14	0.11	0.01	449.48	0.23	0.22
<i>TN mean</i>	0.51	-7.13	3.65	0.15	-0.15	0.36	552.90	0.22	0.21
<i>FP mean</i>	0.65	-5.84	3.15	-0.35	0.25	-0.26	386.27	0.24	0.23
<i>Shanghai</i>									
<i>TP1 (1228)</i>	0.81	-3.44	1.79	-0.16	-0.55	-2.25	415.59	0.35	0.35
<i>TP2 (135)</i>	0.81	-3.10	1.71	-0.12	-0.66	-2.08	422.04	0.36	0.36
<i>TP3 (689)</i>	0.81	-2.95	1.59	-0.17	-1.28	-2.29	472.74	0.36	0.35
<i>TP4 (355)</i>	0.81	-3.52	1.82	0.03	-0.57	-2.74	411.96	0.35	0.35
<i>FN1 (102)</i>	0.82	-3.33	1.80	-0.67	-0.36	-0.14	409.55	0.35	0.35
<i>FN2 (113)</i>	0.80	-3.64	1.84	-0.34	-0.51	-1.21	423.09	0.35	0.34
<i>FN3 (370)</i>	0.80	-3.47	1.80	-0.41	-0.42	-0.84	421.36	0.35	0.35
<i>FN4 (7)</i>	0.80	-2.82	1.39	-1.19	-2.18	3.63	596.53	0.36	0.36
<i>TN mean</i>	0.77	-3.29	1.57	-2.86	1.40	0.62	739.75	0.31	0.32
<i>FP mean</i>	0.82	-3.26	1.71	-0.48	-0.85	-2.26	438.55	0.35	0.35



454 5 Summary and Conclusions

455 Following an earlier preliminary attempt for hazes in Singapore, a deep convolutional neural
456 network containing more than 20 million parameters, namely HazeNet, has been further
457 developed to test forecasting the occurrence of severe haze events during 1979-2019 in two
458 metropolitans of Asia, Beijing and Shanghai. By training the machine to recognize regional
459 patterns of meteorological and hydrological features associated with haze events, the study
460 would advance our knowledge about this still poorly known environmental extreme. The deep
461 CNN has been trained in a supervised learning procedure using the time sequential maps of up to
462 16 meteorological and hydrological variables or features as inputs and surface visibility
463 observations as the labels.

464 Even with a rather limited samples (14,975), the trained machine has displayed a reasonable
465 performance measured by commonly adopted validation metrics. Its performance is clearly better
466 during months with high haze frequency, *i.e.*, all months except dusty April and May in Beijing
467 and from late autumn through entire winter in Shanghai. Relatively larger spatial patterns appear
468 to be more effective than the smaller ones to influence the performance of forecasting. On the
469 other hand, in-depth analysis on performance results has also indicated certain limitations of
470 current approach of solely using meteorological and hydrological data in performing forecast.

471 The trained machine has also been used to examine the sensitivity of the CNN to various
472 input features and thus to identify then remove features ineffective to the performance of the
473 machine. In addition, in order to further categorize typical regional weather and hydrological
474 patterns associated with severe haze versus non-haze events, an unsupervised cluster analysis has
475 been subsequently conducted, benefited from using features with greatly reduced dimensionality
476 produced by the trained machine.

477 The cluster analysis has, arguably for the first time, successfully categorized major regional
478 meteorological and hydrological patterns associated with severe haze and non-haze events in
479 Beijing and Shanghai into a limited number of representative groups, with the typical feature
480 patterns of these clustered groups derived. It has found that the typical weather and hydrological
481 regimes of haze events in Beijing and Shanghai are rather stable conditions, represented by
482 increasing relative humidity, low planetary boundary layer, mild daily temperature change that
483 likely associated with low cloud cover over the haze occurring regions, The result has further
484 revealed a rather strong similarity between the meteorological and hydrological patterns
485 associated with haze events and those with either false alarm or missing forecast prediction
486 outcomes, implying that factors other than meteorological and hydrological ones such as energy
487 consumption variations, long range transport of aerosols, or beyond, could cause haze events to
488 occur even under unfavorable weather conditions.

489 Due to the exploratory nature of this specific effort, several aspects could be further
490 optimized including the rather arbitrary though statistically meaningful labeling. Also, an in-
491 depth analysis on weather regimes exceeds the extent of this paper. Nevertheless, this study has
492 demonstrated the potential of applying deep CNNs with extensive multi-dimensional and time
493 sequential environmental images to advance our understandings about poorly known
494 environmental and weather extremes. The methodology, results alongside experience obtained
495 from this study could benefit future improvement of the skills. Besides, the trained machines can
496 be used in many other types of machine learning and deep learning applications as partially
497 demonstrated here.



498 Appendix A. Performance metrics

499 Several commonly used performance metrics have been used in this study. They are largely derived based on
 500 the so-called confusion matrix (e.g., Swets, 1988) as defined in the following Table A.
 501

502 **Table A.** Confusion matrix for measuring the prediction outcomes of a given class.

Predicted	Observed		
		Positive	Negative
	Positive	True Positive or TP	False Positive or FP
Negative	False Negative or FN	True Negative or TN	

503 Here, *positive* or *negative* is referring to the outcome of a given event or class in the classification, e.g., severe haze
 504 or non-haze events. Hence, the prediction outcome TP is a correct forecast of a severe haze while TN a correct
 505 forecast of a non-haze event, FP represents a false alarm, and FN a missing forecast. The context of outcomes
 506 changes when the designated class is switched. The major performance metrics used in this paper include:

$$507 \quad accuracy = \frac{TP+TN}{N} \quad (A1)$$

$$508 \quad precision = \frac{TP}{TP+FP} \quad (A2)$$

$$509 \quad recall = \frac{TP}{TP+FN} \quad (A3)$$

$$510 \quad F1 \text{ score} = 2 \cdot \frac{precision \cdot recall}{precision+recall} \quad (A4)$$

$$511 \quad ETS = \frac{TP - Hit_{random}}{TP+FP+FN - Hit_{random}}; \quad (A5a)$$

$$512 \quad \text{where: } Hit_{random} = \frac{(TP+FN) \cdot (TP+FP)}{N} \quad (A5b)$$

$$513 \quad HSS = \frac{2 \cdot (TP \cdot TN - FP \cdot FN)}{(TP+FP) \cdot (FP+TN) + (TP+FN) \cdot (TP+TN)} \quad (A6)$$

514 Note that *accuracy* has the same value for all the classes and thus is a good metrics for the overall classification.
 515 Values of all the other metrics differ depending on the referred specific class. Here, *F1 score* is the F-score with $\beta =$
 516 1 (van Rijsbergen, 1974), *ETS* represents equitable threat score (or Gilbert skill score; Gilbert, 1884; range = [-1/3,
 517 1]), *HSS* represents Heidke skill score (Heidke, 1926; range = [-∞, 1]), and *N* is the number of total outcomes.

518 Appendix B. Examining the network's sensitivity to features using trained machine

519 A method has been adopted in this study to use a trained machine from basic training to examine the sensitivity
 520 of the network to a random perturbation applied to the values of different features. The saved machine contains all
 521 the coefficients in different network layers and can be used to predict output from any of these layers using same
 522 input features for training or validation. The sensitivity of the network to a given feature is determined by comparing
 523 the prediction using input feature maps containing randomly perturbation applied to the map of this feature with the
 524 prediction using original input feature maps, and measured by the content loss between these two predictions, with
 525 *img1* with $M \times N$ pixels as the unperturbed and *img2* as perturbed network output:

$$526 \quad Content \text{ Loss} = \frac{1}{M \times N} \sum_{i,j}^{M,N} (img1_{i,j} - img2_{i,j})^2 \quad (B1)$$

527 The perturbation is applied as random patch with addition of -0.2 or 0.2 to 10% of the pixels of the input map of
 528 the targeted feature in each sample while maps of all the other features remain unperturbed. To reduce the workload,
 529 only validation input set corresponding to the class-1 events (about 1020 samples) are used. Therefore, the
 530 sensitivity tested here is actually the sensitivity of the network to a given feature in predicting class-1 events. To
 531 preserve the spatial information of the perturbation field, the output of the 9th layer, or the MaxPooling layer
 532 following the second convolutional layer (Fig. 1) is used as the prediction. It has a size of (15, 31, 92) for Beijing
 533 cases and (15, 15, 92) for Shanghai cases when a kernel size of 20x20 is adopted. A higher content loss represents
 534 that the performance of the network is more sensitive to the variations in value of this feature.



535 Appendix C. Cluster analysis

536 The cluster analysis of this study was conducted in the following three steps (see also Fig. 6).

537 (i) Firstly, the trained and saved HazeNet for both Beijing and Shanghai cases with 9 input features have been
538 used to perform prediction using the entire 14975 input samples in original raw data format, *i.e.*, with a feature
539 volume size of 96x64x9 for Beijing and 64x64x9 for Shanghai for each sample. The prediction results were then
540 summarized into various outcomes, *e.g.*, as true positive (TP), true negative (TN), false positive (FP), or false
541 negative (FN) in referring to the haze class. In the meantime, the output of the second dense layer just before the
542 output layer or latent space (see Fig. 1 & Fig. 6) were further used to form the new data of each sample with reduced
543 feature volume of 512. This new dataset with 14075 samples and 512 feature volume were ready for clustering.

544 (ii) The second step is to actually perform clustering using the new data with reduced size resulted from the
545 previous step. For this purpose, it should be conducted separately for different types of samples or events, *e.g.*,
546 categorizing all the samples for haze into characteristic groups with similarity and same for non-haze events. In
547 order to provide additional information to further the understanding of the network's performance, the clustering
548 was actually conducted for different prediction outcomes, by taking corresponding samples from the new dataset. In
549 this case, TP plus FN would lead to haze events, and TN plus FP to non-haze events. The clustering calculations
550 were done by directly using the k-mean (Steinhaus, 1957) function of scikit-learn library ([https://scikit-](https://scikit-learn.org/stable/modules/clustering.html#clustering)
551 [learn.org/stable/modules/clustering.html#clustering](https://scikit-learn.org/stable/modules/clustering.html#clustering)). For Beijing cases, the trained machine with 9 features
552 produced 2591 TP, 11368 TN, 508 FP, and 508 FN outcomes, and 2407 TP, 11484 TN, 492 FP, and 592 FN for
553 Shanghai. The cluster analysis was performed separately for each of these outcomes in an unsupervised learning
554 procedure to let the machine to categorize corresponding samples into groups based on similarities among them. In
555 practice, similarity is judged by the so-called inertia for a cluster with members of x_i and mean of μ :

$$556 \textit{inertia} = \sum_i^N (\|x_i - \mu\|)^2 \quad (\text{C1})$$

557 The clustering is to seek a grouping with minimized inertia within each cluster. The overall measure is the
558 summation inertia that decreases almost exponentially with the increase of number of clusters. In practice, the
559 cluster analysis was first tested with various given number of clusters ranging from 1 to 100, to examine the values
560 alongside decay of the inertia. This provided a base to identify the smallest possible number of cluster centers with
561 reasonably low inertia in actual cluster analysis. This has actually been decided by using square root of the inertia
562 weighted by the number of samples to put the varying number of samples across various outcomes in consideration.
563 An optimized number of clusters was chosen with a weighted inertia lower than 1/e of that of the single cluster case.
564 For TN, due to the large sample number, this criterion was set to be half of 1/e. As a result, the optimized numbers
565 of clusters for TP, FN, FP, and TN outcomes are 4, 5, 4, and 15 for Beijing and 4, 4, 3, and 10 for Shanghai,
566 respectively,

567 (iii) The members of each cluster derived from (ii) were recorded by the actual sample indices with date
568 attribute. Therefore, actual samples of input data grouped into various clusters can be thus conveniently identified
569 with corresponding feature maps retrieved, either in the format of normalized or unnormalized (*i.e.*, in original
570 quantity as in reanalysis dataset), and used for further analyses. In practice, cluster-averaged maps for various
571 features were performed beforehand.

572 Code and data availability

573 The Python script for network architecture, training and validation is rather straightforward and simple,
574 basically consisting of directly adopted function calls from Keras interface library ([https://github.com/keras-](https://github.com/keras-team/keras)
575 [team/keras](https://github.com/keras-team/keras)) with TensorFlow-GPU (<https://www.tensorflow.org>) as backend, or from scikit learn library
576 (<https://scikit-learn.org/>). All the data used for analyses are publicly available as indicated in the
577 Acknowledgements.

578 Competing interests

579 The author declares that he has no conflict of interest.

580



581 Acknowledgements

582 This study is supported by L'Agence National de la Recherche (ANR) of France under "Programme
583 d'Investissements d'Avenir" (ANR-18-MPGA-003 EUROACE). The author thanks the European Centre for
584 Medium-range Weather Forecasts for making the ERA5 data publicly available under a license generated and a
585 service offered by the Copernicus Climate Change Service, and the National Center for Environmental Information
586 of the US NOAA for making GSOD data available. All the related computations have been accomplished using the
587 GPU clusters of French Grand equipment national de calcul intensif (GENCI) (Project 101056) and the CNRS
588 Mesocenter of Computing of CALMIP (Project p18025).

589 References

- 590 Chan, C. K. and Yao, X.: Air pollution in mega cities in China, *Atmos. Environ.*, 42, 1-42, 2008.
591 Chattopadhyay, A., Nabizadeh, E. and Hassanzadeh, P.: Analog forecasting of extreme-causing
592 weather patterns using deep learning. *J. Adv. Modeling Earth Sys.*, 12, e2019MS001958.
593 Doi:/10.1029/2019MS001958, 2020.
- 594 Forest, D.: *Generative Deep Learning*, O'Reilly Media, Inc., 2019.
- 595 Gagne, D., Haupt, S. and Nychka, D.: Interpretable deep learning for spatial analysis of severe
596 hailstorms. *Mon. Wea. Rev.*, 147, 2827–2845, Doi:/10.1175/MWR-D-18-0316.1, 2019.
- 597 Gilbert, G. K.: Finley's tornado predictions, *Amer. Meteor. J.*, 1, 166–172, 1884.
- 598 Goodfellow, I., Bengio, Y. and Courville, A.: *Deep Learning*, MIT Press, 800pp., 2017.
- 599 Grover, A., Kapoor, A. and Horvitz, E.: A deep hybrid model for weather forecasting, *Proc. 21st*
600 *ACM SIGKDD Intern'l Conf. KDD*, p.379-386, Sydney, Australia, August 10, 2015. ACM.
601 ISBN 978-1-4503-3664-2/15/08. Doi:10.1145/2783258.2783275, 2016.
- 602 He, K., Zhang, X., Ren, S. and Sun, J.: Deep residual learning for image recognition,
603 arXiv:1512.03385, 2015.
- 604 Heidke, P.: Calculation of the success and goodness of strong wind forecasts in the storm
605 warning service, *Geogr. Ann. Stockholm*, 8, 301–349, 1926.
- 606 Hersbach, H., Bell, B., Berrisford, P., Hirahara, S., Horányi, A., Muñoz-Sabater, J., Nicolas, J.,
607 Peubey, C., Radu, R., Schepers, D., Simmons, A., Soci, C., Abdalla, S., Abellan, X.,
608 Balsamo, G., Bechtold, P., Biavati, G., Bidlot, J., Bonavita, M., De Chiara, G., Dahlgren, P.,
609 Dee, D., Diamantakis, M., Dragani, R., Flemming, J., Forbes, R., Fuentes, M., Geer, A.,
610 Haimberger, L., Healy, S., Hogan, R. J., Hólm, E., Janisková, M., Keeley, S., Laloyaux, P.,
611 Lopez, P., Lupu, C., Radnoti, G., de Rosnay, P., Rozum, I., Vamborg, F., Villaume, S. and
612 Thépaut, J.-N.: The ERA5 global reanalysis, *Q. J. R. Meteorol. Soc.*, 146, 1999–2049, 2020.
- 613 Ioffe, S. and Szegedy, C.: Batch normalization: Accelerating deep network training by reducing
614 internal covariate shift, arXiv:1502.03167, 2015.
- 615 Jiang, G.-Q., Xu, J. and Wei, J.: A deep learning algorithm of neural network for the
616 parameterization of typhoon-ocean feedback in typhoon forecast models, *Geophys. Res. Lett.*,
617 45, <https://doi.org/10.1002/2018GL077004>, 2018.
- 618 Kiehl, J. T. and Briegleb, B. P.: The relative roles of sulfate aerosols and greenhouse gases in
619 climate forcing, *Science*, 260, 311-314, 1993.
- 620 Kurth, T., Treichler, S., Romero, J., Mudigonda, M., Luehr, N., Phillips, E., Mahesh, A.,
621 Matheson, M., Deslippe, J., Fatica, M., Prabhat and Houston, M.: Exascale deep learning for
622 climate analytics, arXiv:1810.01993, 2018.
- 623 Lagerquist, R., McGovern, A. and Gagne II, D.: Deep learning for spatially explicit prediction of
624 synoptic-scale fronts. *Wea. Forecasting*, 34, 1137–1160. Doi:10.1175/WAF-D-18-0183.1,
625 2019.



- 626 LeCun, Y., Bengio, Y. and Hinton, G.: Deep learning, *Nature*, 521, 436–444,
627 doi:10.1038/nature14539, 2015.
- 628 Lee, H.-H., Iraqui, O. and Wang, C.: The impacts of future fuel consumption on regional air
629 quality in Southeast Asia, *Sci. Rep.*, 9:2648, doi:10.1038/s41598-019-39131-3, 2019.
- 630 Lee, H.-H., Iraqui, O., Gu, Y., Yim, H.-L. S., Chulakadabba, A., Tonks, A. Y. M., Yang, Z. and
631 Wang, C.: Impacts of air pollutants from fire and non-fire emissions on the regional air
632 quality in Southeast Asia, *Atmos. Chem. Phys.*, 18, 6141–6156, doi:10.5194/acp-18-6141-
633 2018, 2018.
- 634 Lee, H.-H., Bar-Or, R. and Wang, C.: Biomass Burning Aerosols and the Low Visibility Events
635 in Southeast Asia, *Atmos. Chem. Phys.*, 17, 965–980, doi:10.5194/acp-17-965-2017, 2017.
- 636 Lin, Y., Wijedasa, L. S. and Chisholm, R. A.: Singapore’s willingness to pay for mitigation of
637 transboundary forest-fire haze from Indonesia, *Environ. Res. Lett.*, 12, 024017,
638 doi:10.1088/1748-9326/aa5cf6, 2016.
- 639 Liu, M., Huang, Y., Ma, Z., Jin, Z., Liu, X., Wang, H., Liu, Y., Wang, J., Jantunen, M., Bi, J. and
640 Kinney, P. L.: Spatial and temporal trends in the mortality burden of air pollution in China:
641 2004–2012, *Environ. Int.*, 98, 75–81, 2017.
- 642 Liu, Y., Racah, E., Prabhat, Correa, J., Khosrowshahi, A., Lavers, D., Kunkel, K., Wehner, M.
643 and Collins, W.: Application of deep convolutional neural networks for detecting extreme
644 weather in climate datasets. arXiv:1605.01156, 2016.
- 645 McGovern, A., Lagerquist, R., Gagne II, D. J., Jergensen, G. E., ElmLMore, K. L., Homeyer, C.
646 R. and Smith, T.: Making the black box more transparent: Understanding the physical
647 implications of machine learning, *Bull. Amer. Meteor. Soc.*, 100, 2175–2199, 2019.
- 648 Ronneberger, O., Fischer, P. and Brox, T.: U-Net: Convolutional networks for biomedical image
649 segmentation, arXiv:1505.04597, 2015.
- 650 Shi, X., Chen, Z., Wang, H. and Yeung, D.-Y.: Convolutional LSTM network: A machine
651 learning approach for precipitation nowcasting, arXiv:1506.04214, 2015.
- 652 Silva, R. A., West, J. J., Zhang, Y., Anenberg, S. C., Lamarque, J.-F., Shindell, D. T., Collins,
653 W. J., Dalsoren, S., Faluvegi, G., Folberth, G., Horowitz, L. W., Nagashima, T., Naik, V.,
654 Rumbold, S., Skeie, R., Sudo, K., Takemura, T., Bergmann, D., Cameron-Smith, P., Cionni,
655 I., Doherty, R. M., Eyring, V., Josse, B., MacKenzie, I. A., Plummer, D., Righi, M.,
656 Stevenson, D. S., Strode, S. Szopa, S. and Zeng, G.: Global premature mortality due to
657 anthropogenic outdoor air pollution and the contribution of past climate change, *Environ.*
658 *Res. Lett.*, 8, 034005, doi:10.1088/1748-9326/8/3/034005, 2013.
- 659 Simonyan, K. and Zisserman, A.: Very deep convolutional networks for large-scale image
660 recognition, arXiv:1409.1556, 2015.
- 661 Smith, A., Lott, N. and Vose, R.: The integrated surface database: Recent developments and
662 partnerships, *Bull. Amer. Meteorol. Soc.*, 92, 704–708, doi:10.1175/2011BAMS3015.1,
663 2011.
- 664 Steinhaus, H.: Sur la division des corps matériels en parties, *Bull. Acad. Polon. Sci.*, 4, 801–804,
665 1957.
- 666 Swets, J.: Measuring the accuracy of diagnostic systems, *Science*, 240, 1285–1293, 1988.
- 667 Szegedy, C., Vanhoucke, V., Ioffe, S., Shlens, J. and Wojna, Z.: Rethinking the inception
668 architecture for computer vision, arXiv:1512.00567, 2015.
- 669 van Rijsbergen, C., 1974: Foundation of evaluation, *J. Documentation*, 30, 365–373.
- 670 Wang, C.: Exploiting deep learning in forecasting the occurrence of severe haze in Southeast
671 Asia, arXiv:2003.05763, 2020.



672 Weyn, J. A., Durrán, D. R. and Caruana, R.: Improving data-driven global weather prediction
673 using deep convolutional neural networks on a cubed sphere, *J. Adv. Modeling Earth Sys.*,
674 e2020MS002109, <https://doi.org/10.1029/2020MS002109>, 2020.
675
676